Peptide Assembly Integration of Fibroblast-Targeting and Cell-Penetration Features for Enhanced Antitumor Drug Delivery

Tianjiao Ji, Yanping Ding, Ying Zhao, Jing Wang, Hao Qin, Xiaoman Liu, Jiayan Lang, Ruifang Zhao, Yinlong Zhang, Jian Shi, Ning Tao, Zhihai Qin,* and Guangjun Nie**

Nanomedicines, with great potential for minimizing toxicity, increasing bioavailability and/or improving pharmacokinetic features of drugs, have seen enormous development on cancer therapy in the last dacades.[1–5] However, in spite of the promising therapeutic potential exhibited by the numerous antitumor nanomaterials, it remains a major challenge for particulate-based therapeutics to effectively transport into solid tumors.[6–8] Although many multifunctional drug-loaded nanomaterials have been designed to increase drug delivery into tumor cells,[9–12] only limited improvement has been achieved to overcome multilayered stromal cell barrier and membrane barrier of tumor cells.[6–8,13] Thus, an optimal nanomaterial which can break these barriers should hold great promise for increased drug perfusion and therapeutic efficacy in solid tumors, especially in stromal enriched tumors.

Cancer-associated fibroblasts (CAFs), a predominant stromal cell type in the tumor microenvironment,[14–16] have been proved to promote tumor growth and metastasis, induce tumor fibrosis and alter composition and physiochemical properties of extracellular matrix. With fast tumor growth, they will create growth-induced solid stress, impeding the penetration of both macromolecules and nanomedicines.[17–21] Herein, we proposed that targeting and depletion of CAFs could signficantly improve drug delivery in solid tumors. To validate our hypothesis, we developed a dual-mode nanomaterial with the ability of CAFs targeting and efficient cell penetration to achieve tumor-targeted drug delivery, elimination of CAFs and ultimate destruction of tumor cells. Our strategy was confirmed effective to improve the chemotherapeutic drug delivery for the treatment of CAF-rich solid tumors.

To achieve the goal of CAFs targeting and enhanced cell penetration, a novel cell-penetrating peptide (CPP) based amphiphilic peptide (C2KG2R9) monomer was designed and synthesized (**Scheme 1**A). Nine arginine (R9) residues which has been verified to hold superlative cell-penetrating efficiency among reported oligopolyarginines,[22] were engineered at the hydrophilic block of the CPP to provide cationic charges for effective membrane translocation.[22–25] Cholesterol, an important component of cell membrane, was designed to be embedded as the hydrophobic tail, which has been well-documented to drive peptide self-assembly and improve membrane permeability.[26,27] The amphiphilic peptide-cholesterol monomers can readily self-assemble to form core–shell structured peptide nanoparticles (PNP), with a hydrophobic cholesterol core and a hydrophilic cationic R9 peptide shell towards the surrounding aqueous environment (Scheme 1B).[24,28] Hydrophobic antitumor drug doxorubicin (DOX) can be encapsulated by PNP, to form DOX-loaded nanoparticles, PNP-D. The high local density of positive charges conferred cell penetration capacity on PNP-D to realize efficient drug delivery. However, it has been reported that nanomaterials carrying positive surface charges are subject to nonspecific phagocytosis by the reticuloendothelium systems (RES), resulting in short blood circulation time.[29–31] Thus, mouse monoclonal antibody (mAb) molecules targeting human fibroblast activation protein-α (FAP-α), a transmembrane protein selectively expressed by CAFs rather than normal cells,[32–35] were modified onto the surface of PNP-D via electrostatic binding to construct PNP-D-mAb. The surface modification with anti-FAP mAb can shelter the positive charges, which was considered to not only stabilize PNP-D-mAb in blood circulation but also render PNP-D-mAb to specifically recognize CAFs and accumulate in tumor tissues. According to the design features, we proposed that upon arrival at the tumor tissue, PNP-D-mAb was inclined to binding with CAFs through interactions between the surface-attached anti-FAP mAb and the FAP-α expressed on the CAF cell membrane, resulting in the dissociation of mAb from PNP-D and exposure of CPP in the tumor microenvironment. The CPP and cholesterol components further coordinately enhanced the cellular uptake of therapeutic drugs into CAFs, tumor cells and other stromal cells, which will break the stromal barrier, increase drug access to tumor cells, and achieve efficient therapeutic effect (Scheme 1C). Our designed PNP-D-mAb is an ensemble nanoformulation with the function of targeting, penetration, and therapy, which holds great promise for solid tumor treatment.

The employed cationic amphiphilic peptide-cholesterol showed a critical micelle concentration (CMC) of 32.4 mg L^{-1} (13.0×10^{-6} M) in PBS (pH 7.4) (**Figure 1**A). At concentrations above, it could easily self-assemble into core–shell nanoparticles.

T. Ji, Dr. Y. Ding, Dr. Y. Zhao, J. Wang, H. Qin, J. Lang, R. Zhao, Y. Zhang, J. Shi, Prof. G. Nie
CAS Key Laboratory for Biomedical Effects of Nanomaterials and Nanosafety, National Center for Nanoscience and Technology (NCNST)
11 Beiyitiao, Zhongguancun
Beijing 100190, China
E-mail: zhaoying@nanoctr.cn; niegj@nanoctr.cn

X. Liu, Dr. N. Tao, Prof. Z. Qin
CAS Key Laboratory of Protein and Peptide Pharmaceuticals
Institute of Biophysics
15 Datun Road, Beijing 100101, China
E-mail: zhihai@ibp.ac.cn

DOI: 10.1002/adma.201404715

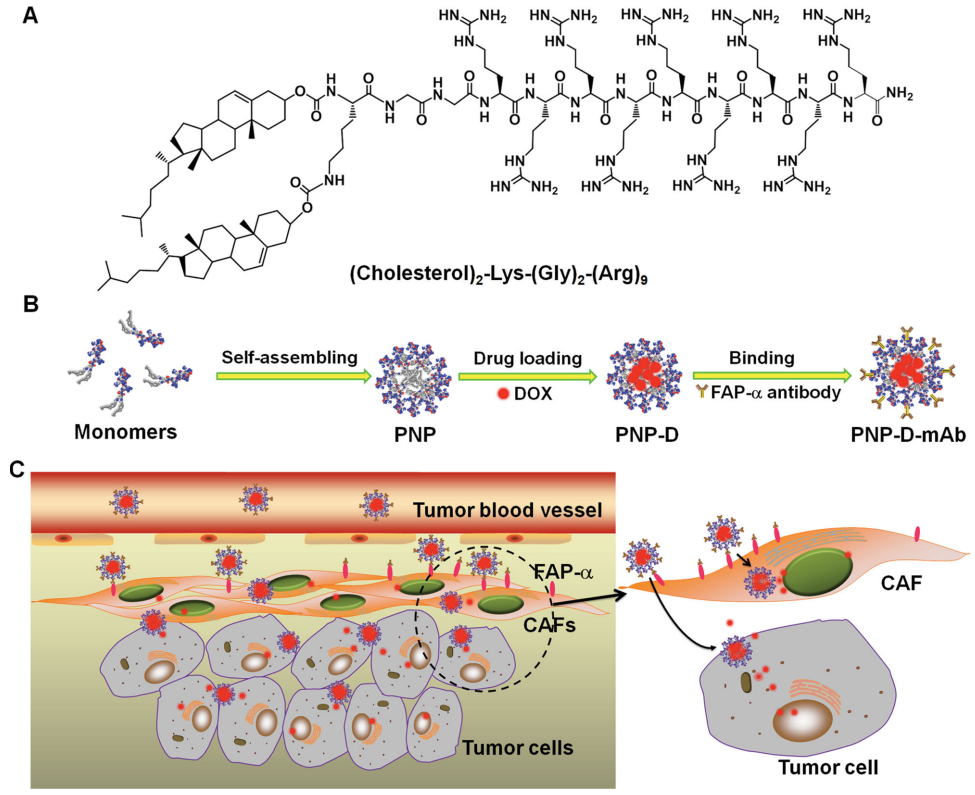

Scheme 1. Design and proposed mechanism of PNP-D-mAb. A) The structure of the cholesterol-modified CPP. B) Schematic illustration of the nanoparticle formation process including peptide assembling, drug loading, and mAb modification. C) The proposed mechanism of PNP-D-mAb in CAFs targeting and drug penetration.

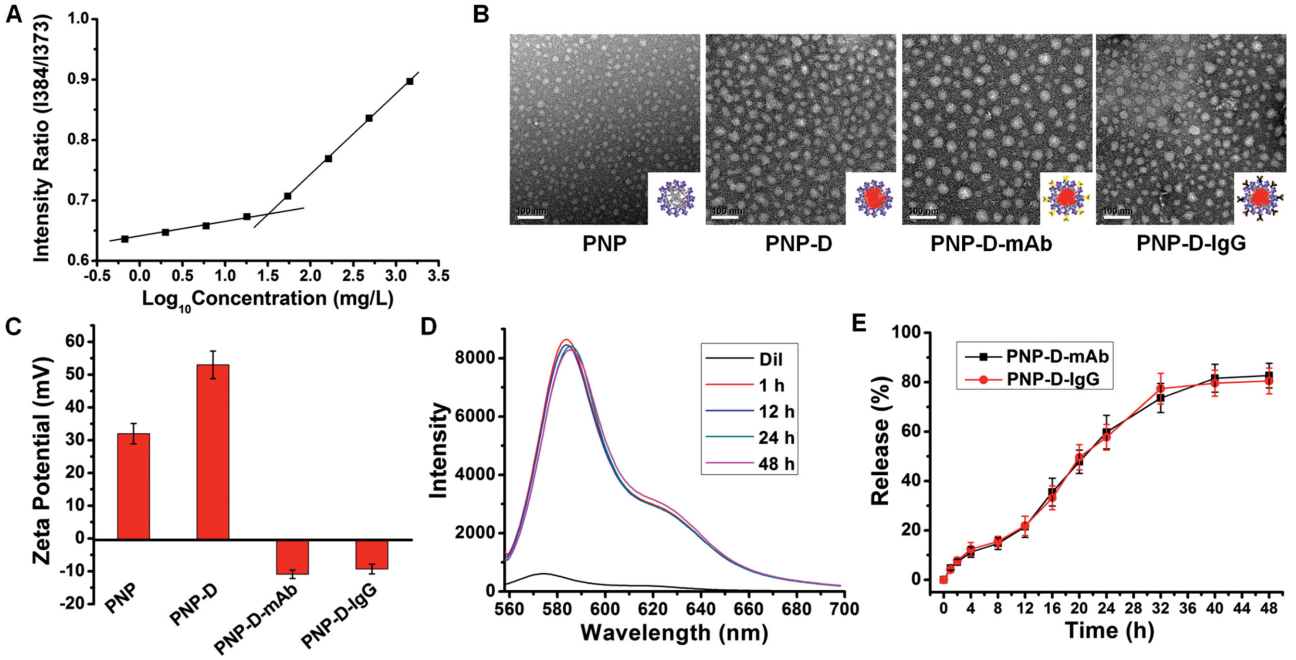

Figure 1. Characterization of cholesterol-modified CPP and their self-assembled nanoparticles (NP). A) Determination of the CMC of the peptide. The peptide can form micelles at the concentration equal to or above 32.4 mg L^{-1} (13.0×10^{-6} M). B) The morphology of PNP, PNP-D, PNP-D-mAb, and PNP-D-IgG by TEM examination. The concentration of peptide in each NP solution was 0.98 mg mL^{-1}. The scale bar is 100 nm. C) Zeta potentials of NPs detected by DLS. D) The fluorescence intensity of Dil inserted in PNP-mAb after incubation with 10% FBS/PBS for different time. The fluorescence intensity did not change during the 48 h incubation. E) The drug release profiles of PNP-D-mAb and PNP-D-IgG in 10% FBS/PBS.

To guarantee the stability of the nanostructures during the dilution in vitro and in vivo, a 30-fold CMC (0.98 mg mL^{-1}) was used in the following experiments. Under this concentration, the peptide-cholesterol formed spherical nanoparticles with diameter about 30 nm (Figure 1B and Figure S1, Supporting Information). When loaded with DOX, their diameter increased to about 45 nm. The final diameter after attachment of anti-FAP mAb (PNP-D-mAb) or IgG molecules (as a control, PNP-D-IgG) was about 60 nm (Figure 1B and Figure S1, Supporting Information). During the drug loading process, the zeta potentials of the nanoparticles in PBS (pH 7.4) also increased from 32.0 ± 3.1 mV (PNP) to 53.1 ± 4.2 mV (PNP-D), while the increasing attachment of negatively charged anti-FAP mAb or IgG molecules gradually reversed the zeta potentials (Figure 1C). When the ratio of mAb/IgG to peptide reached 1:10, the zeta potentials of PNP-D-mAb and PNP-D-IgG turned to −10.9 ± 1.3 and −9.3 ± 1.5 mV (Table S1, Supporting Information), respectively, which retained steady in spite of the increment of mAb or IgG. Therefore, the ratio 1:10 was considered optimal for following studies, at which the highest DOX loading ratio of PNP-D-mAb was 4.94% in weight (Table S2, Supporting Information). To detect the stability of the designed nanoparticles, 1,1′-dioctadecyl-3,3,3′,3′-tetramethylindocarbocyanine perchlorate (Dil, a dye that can only be activated when embedded in micelles, membrane lipid bilayer or liposomes) was encapsulated in the hydrophobic core of PNP-mAb. After incubation with 10% fetal bovine serum (FBS) in PBS for 48 h, the fluorescence intensity remained constant (Figure 1D), demonstrating the integrity of PNP-mAb micelle structure. In addition, the morphology of PNP-D-mAb or PNP-D-IgG did not change when incubated with 10% FBS/PBS for 48 h (Figure S2, Supporting Information), indicating the mAb or IgG molecules were still attached on the PNP surface during the time interval. Meanwhile, only 30% of DOX was released from PNP-D-IgG or PNP-D-mAb in 10% FBS/PBS for 12 h (Figure 1E), suggesting the controlled drug release character of these nanoparticles. The above results demonstrated the successful construction of PNP-D-mAb, which exhibited uniform nanostructure with suitable size and surface charges, favorable stability, as well as controlled drug release. The proper size range in the sub-100-nm is optimal to harness the enhanced permeability and retention (EPR) effect for passive tumor targeting.[36,37] Specific targeting of surface anti-FAP-α mAbs to CAFs, the major stromal cells surrounding tumor tissues, will further enhance the targeting ability of the nanoparticle, with promise for increased therapeutic efficacy in vitro and in vivo.

To confirm the targeting specificity and the cell penetration efficiency of the designed nanomaterial, we incubated PNP-D, PNP-D-IgG, and PNP-D-mAb (DOX concentration, 1×10^{-6} M) with CAFs, PC-3 (a prostate cancer cell line), and human umbilical endothelial cells (HUVECs) at 4 °C. The immunofluorescence and western blot results (**Figure 2**A, Figure S3, Supporting Information) demonstrated that FAP-α was specifically expressed on CAFs instead of PC-3 cells and HUVECs. It has been reported that low temperature (4 °C) inhibits endocytosis.[38] Since multiple pathways exist for CPPs to enter cells, significant amount of CPP nanostructures still penetrated into cells after inhibition of endocytic pathways.[39,40] Consistent with previous reports, all three types of cells in the PNP-D treated groups exhibited significant fluorescence of DOX (Figure 2B), indicating the efficient cellular penetration ability of PNP-D. As absorption of IgG molecules shielded the function of CPP, PNP-D-IgG could not be taken up by cells at 4 °C, therefore, neither cell type showed DOX fluorescence after PNP-D-IgG treatment. In contrast, PNP-D-mAb only induced strong DOX signal in CAFs but not PC-3 or HUVECs (Figure 2B). These results illustrated that PNP-D-mAb specifically targeted CAFs and enabled effective DOX delivery into CAFs, which suggested that PNP-D-mAb interacted with CAFs in a different pattern from with PC-3 cells or HUVECs.

To investigate the underlying mechanism, we labeled the anti-FAP mAb with carboxyfluorescein-5-succimidyl ester (FAM) and the hydrophobic core of PNP with Dil, respectively, and finally obtained the dual-labeled PNP-mAb nanostructure. After incubation with CAFs, PC-3 or HUVECs at 37 °C for 4 h, we detected the localization of mAb and PNP by confocal microscopy. Interestingly, we observed that almost all PNPs were colocalized with mAbs and were not taken up by either PC-3 or HUVECs (Figure S4A, Supporting Information). In contrast, after incubation with CAFs, the majority of PNPs was dissociated with the mAbs and entered cells effectively, whereas almost all FAP-α mAbs remained on the cell surface (Figure S4B, Supporting Information). These results demonstrated that anti-FAP mAbs can be detached from PNP once specifically bound to FAP-α on CAFs, which enabled the dissociated CPP and cholesterol components to facilitate the cellular penetration of the nanostructures. However, anti-FAP mAbs could not depart from PNP after incubation with FAP-α negative cell lines, PC-3, and HUVECs, leading to low cellular uptake of PNP. From these observations, we deduced that the interaction between the antibody and antigen was higher than the electrostatic force between PNP nanostructure and the antibody. This difference of binding capacity may contribute to the dual-mode targeting and penetration. In addition, when we incubated PC-3 with the conditioned culture medium from CAFs treated by the labeled PNP-mAb, intense Dil fluorescence signal appeared intracellularly (Figure S4B, Supporting Information), indicating that PNP can be taken up by PC-3 only after extricated from mAbs which already interacted with FAP-α on CAFs. To further evaluate the role of CPP in cellular uptake of PNP-mAb, a control peptide (CP: C2KG2S2QS2QR3) (Figure S5A, Supporting Information) was designed. TEM examination showed that CP formed similar nanostructure with PNP-mAb after absorption of anti-FAP mAbs (CPNP-mAb) (Figure S5B, Supporting Information). Although CPNP-mAb can recognize the CAFs, the low cell-penetrating capability of CP restricted the uptake of CPNP by CAFs (Figure S5C, Supporting Information), suggesting that the efficient cellular uptake of PNP-mAb were primarily contributed by dissociated PNP rather than FAP-α receptor-mediated internalization.[22] The aforementioned studies revealed the mechanism underlying the targeting and penetration of PNP-mAb: when encountering CAFs, the anti-FAP mAbs decorated on PNP-mAb dissociated with PNP due to strong interaction with FAP-α selectively expressed on the CAF surface, resulting in the exposure of PNP and subsequent cellular penetration coordinated by the CPP and cholesterol components.

CAFs and tumor cells are simutaneously present in most solid tumors. To imitate this feature in vitro, a cell coculture system was used by cultivating CAFs with CellTrace Calcein

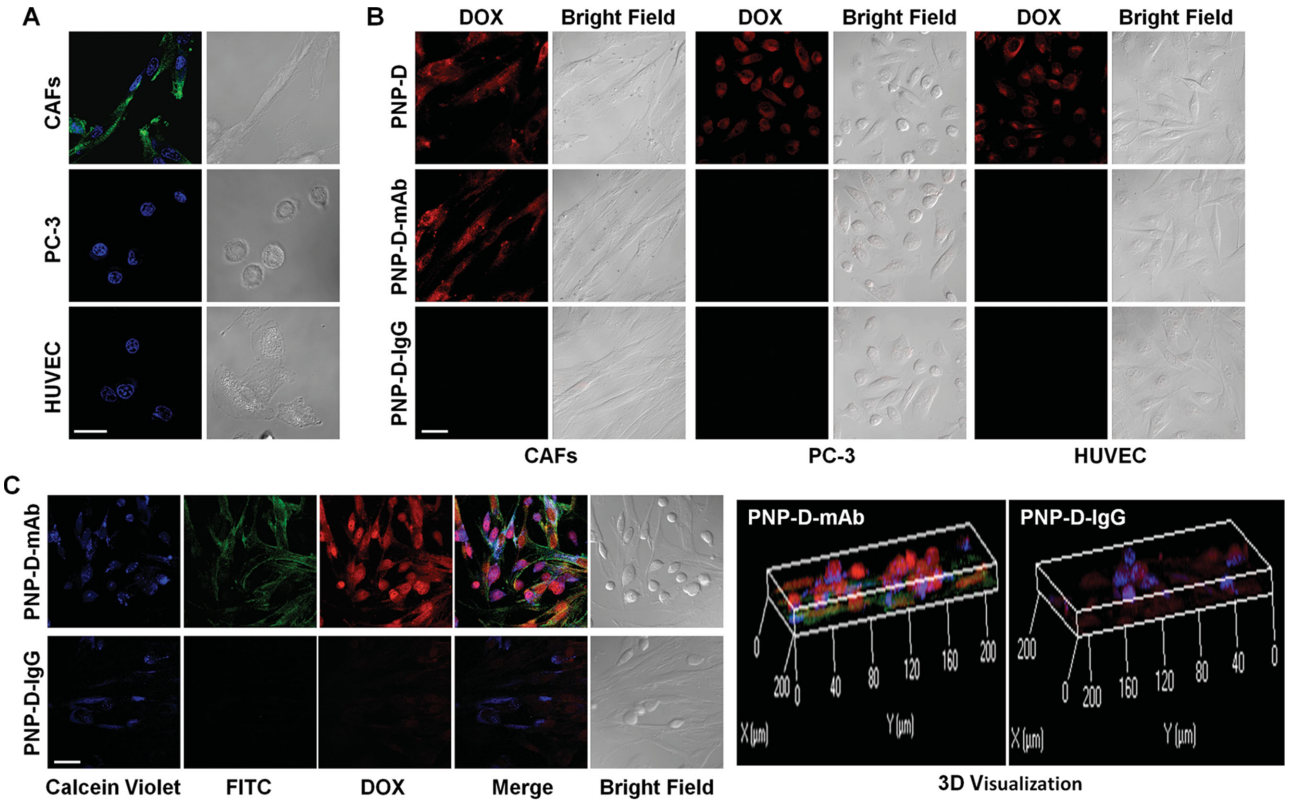

Figure 2. Cellular targeting and penetrating efficiency of DOX with different formulations. A) Immunofluorescence analysis for the expression of FAP-α in CAFs, PC-3, and HUVECs. Scale bar, 50 μm. B) Targeting and penetration of DOX-loaded NPs by confocal microscopy. CAFs, PC-3, and HUVECs were incubated with PNP-D, PNP-D-IgG or PNP-D-mAb, respectively, at 4 °C for 1 h, followed by fixation and detection for DOX signal (560–650 nm, red) by confocal microscopy. The concentration of DOX in each formulation was 1×10^{-6} M. Scale bar, 50 μm. C) Targeting and uptake of PNP-D-mAb in CAFs and PC-3 cocultured system. PC-3 cells labeled with CellTrace Calcein Violet, AM were cocultured with CAFs and treated by PNP-D-mAb or PNP-D-IgG at 37 °C for 4 h, followed by incubation with goat anti-mouse FITC-conjugated IgG to track decorated mAb or IgG. The fluorescent signals were measured by confocal microscopy. Blue: CellTrace Calcein Violet, AM; green: FITC; red: DOX. The scale bar is 50 μm (left). 3D visualization of the coculture system by confocal microscopy was shown right. In PNP-D-mAb treated group, most FITC signal located in the CAFs, which were thinner than the PC-3 cells. In PNP-D-IgG treated group, no FITC fluorescence and marginal DOX signal were detected.

Violet labeled PC-3 cells. After treated by PNP-D-mAb or PNP-D-IgG at 37 °C for 4 h, the cells were incubated with FITC-conjugated goat anti-mouse IgG to track the anti-FAP mAb. In PNP-D-mAb treated group, the FITC signal was mainly distributed on the membrane of the CAFs, whereas significant intracellular DOX signal emerged in both cell types (Figure 2C). The 3D visualization also demonstrated that most FITC signal located in the CAFs, which were thinner than the PC-3 cells (Figure 2C). In contrast, no FITC fluorescence and marginal DOX signal were detected in PNP-D-IgG treated group. These results demonstrated that when PNP-D-mAb recognized CAFs in the coculture system, the mAb bound to FAP-α on CAF surface and detached from PNP-D, causing the exposure of CPP and cholesterol elements which mediated the effective transport of DOX across cell membranes of both PC-3 cells and CAFs. Taken together, the above in vitro studies verified the specific targeting and enhanced cell penetration capacity of PNP-D-mAb, which are preferential characteristics for antitumor therapy.

To further quantitatively measure the cellular uptake of these drug formulations, free DOX and three nanoparticles were incubated with CAFs, PC-3 and HUVECs at 37 °C for 4 h, and their cellular uptake indicated by DOX autofluorescence was measured by flow cytometry (**Figure 3**A). PNP-D without specificity exhibited higher efficiency to enter all cell types than free DOX, demonstrating that the cell penetration mediated by the CPP and cholesterols based nanoparticles was an efficient strategy for drug delivery into cells. The IgG molecules shielded positive charges of CPP, and therefore PNP-D-IgG showed the lowest intracellular signal in all cells. However, compared to PNP-D, PNP-D-mAb further enhanced the intracellular fluorescence only when treating CAFs, but exhibited similarly low fluorescence signal as PNP-D-IgG in FAP-α negative cells (PC-3 cells and HUVECs). The same phenomenon could also be drawn from laser confocal microscopy analysis (Figure 3B). At the same excitation intensity, PNP-D-mAb showed the highest penetration efficiency for CAFs. The possible reason was that the CAFs-targeting ability of anti-FAP mAb increased the opportunity for PNP-D-mAb to accumulate around CAFs compared to the nontargeting nanoparticles and caused the exposure of PNP-D which efficiently delivered DOX into cells. These results concluded that PNP-D-mAb achieved

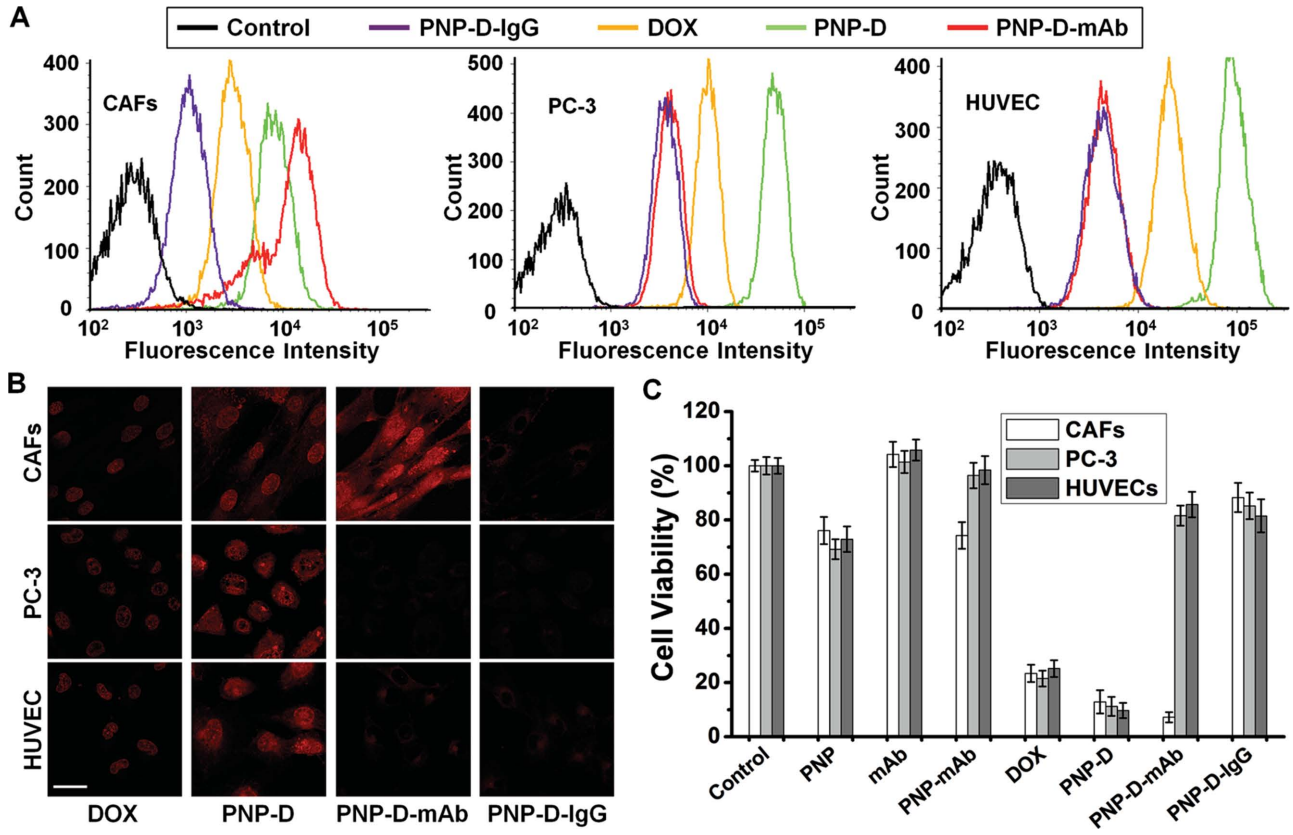

Figure 3. Quantitative analysis of cellular uptake and cytotoxicity of the nanoparticles. A) Flow cytometry measurement of internalized DOX signals in cells. CAFs, PC-3, and HUVECs were incubated with DOX, PNP-D, PNP-mAb, and PNP-IgG, respectively. After washing and permeabilization, cells were analyzed by flow cytometry. The concentration of DOX in each component was 1×10^{-6} M. Control indicated untreated cells. B) Confocal images of internalized DOX with different formulations in cells. Red: DOX. The scale bar is 50 μm. Cells were treated similarly as they were in flow cytometry analysis, and the fluorescence intensity was consistent with that in flow cytometry. C) Cytotoxicity of different DOX formulation and nanomaterial components to the three cell types. Cells were treated at 37 °C for 24 h and analyzed by CCK-8 kit. The concentration of DOX in each formulations was 5×10^{-6} M.

the targeting specificity to CAFs through the antibody–antigen interaction and enhanced drug penetration mediated by CPP and cholesterols based nanoparticles.

Since the cell transport efficiency of DOX is a major determinant of its cytotoxicity, we further detected the effect of various DOX formulations on the viability of CAFs, PC-3, and HUVECs. The final DOX concentration was 5×10^{-6} M which was proved effective for the induction of cell death (Figure S6, Supporting Information). 24 h after treatment, the amounts of viable cells were evaluated by a cell counting kit-8 (CCK-8). The PNP showed a certain degree of toxicity to all the three cell types probably because of its positively charged surface which has been reported destructive to cell membrane (Figure 3C).[41,42] The PNP-D, being loaded with the chemotherapeutic drug and maintaining the positive surface charge, exhibited much greater cytotoxicity to all the cells compared to PNP. By attaching negatively charged molecules (IgG molecules or anti-FAP mAb) to the surface, the apparent net charges of nanoparticles were reversed and their nonspecific cell uptake was reduced. Hence, both PNP-D-IgG and PNP-D-mAb showed low toxicity to FAP-α negative cells (PC-3 cells and HUVECs). However, for FAP-α positive cells, CAFs, PNP-D-mAb showed even higher killing efficiency than PNP-D, which was corresponding to the amount of acquired DOX. Consequently, the PNP-D-mAb represented targeting specificity and significant cytotoxicity, raising possibilities of further application in vivo.

The successful application of nanoformulations requires high stability in blood circulation and specific accumulation at the disease site. Therefore, we measured the stability in circulation, blood clearance rate and biodistribution of PNP-mAb prior to utilization in vivo. We labeled anti-FAP mAbs with a near-infrared dye Cy5.5, and labeled the hydrophobic core of NPs with Dil. Normal BALB/c mice (n = 4) were intravenously injected with Cy5.5, Cy5.5-mAb, and dual-labeled PNP-mAb (Cy5.5-PNP-Dil-mAb, the peptide dose: 100 μL, 0. 98 mg mL^{-1}), respectively. At different time points, blood was collected and detected for fluorescence signal by Maestro in vivo imaging system (Figure S7A, Supporting Information). Based on the relative fluorescence intensity (RFI) shown in Figure S7B (Supporting Information), the half-life of Cy5.5-PNP-Dil-mAb was about 3 h (RFI: 42.2% ± 3.3%), while the RFI of Cy5.5 and Cy5.5-mAb were only 10.0% ± 2.6% and 33.6% ± 3.8%, respectively, 1 h after injection. Meanwhile, the Dil signal (free Dil cannot be detected in blood) was corresponding with Cy5.5 signal in Cy5.5-PNP-Dil-mAb treated group, indicating the circulating stability of PNP-mAb system. For further exploration

of biodistribution, we intravenously injected the Cy5.5-PNP-mAb to mice bearing CAFs and PC-3 coimplanted prostate tumors and measured in vivo Cy5.5 fluorescence over different time post injection (Figure S8, Supporting Information). At the beginning (5 min after injection), the fluorescence distributed all through the body. As time increasing, nonspecific fluorescent signal across the body decreased gradually, but the signal at the tumor site steadily increased. At 12 h, most fluorescence signal in the body accumulated at the tumor site. The ex vivo imaging of major organs showed that most signal was located at the tumor except for a certain degree of signal on the liver (Figure S8B,C, Supporting Information). The signal intensity at the tumor site gradually decreased and disappeared up to 72 h. These observations illustrated that PNP-mAb system was stable in the blood circulation during the first 12 h and can specifically accumulate at the tumor site, potentiating the application of PNP-D-mAb for tumor treatment.

An optimal nanomaterial is expected to possess high tumor specificity and enhanced drug penetration. To further explore the tumor specificity and penetration of PNP-D-mAb in vivo, Cy5.5 labeled PNP-D-IgG and PNP-D-mAb were intravenously injected to mice bearing CAFs and PC-3 coimplanted tumors. All the nanoformulations contained the same amount of peptide (100 μL, 0.98 mg mL^{-1}) and DOX (5 mg kg^{-1}), equal mass of IgG molecules or mAb, and similar Cy5.5 fluorescence intensity (Figure S9, Supporting Information). The fluorescence signal of Cy5.5 in mice was measured 12 h after injection (**Figure 4**A). The weak signal in PNP-D-IgG treated mice may originate from the EPR effect of nanoparticles. Compared to PNP-D-IgG treated mice, PNP-D-mAb treated ones showed about 10-fold higher fluorescence intensity at the tumor site, implying high targeted accumulation of PNP-D-mAb in the tumor site. 24 h after injection, tumors were removed from the mice and were frozen-sliced for ex vivo imaging. DOX and Cy5.5 fluorescences were detected by laser confocal microscopy (Figure S10, Supporting Information). In tumors from PNP-D-IgG treated mice, both DOX and Cy5.5 signals were rather weak, and the Cy5.5 fluorescence was distributed without any specificity. In contrast, the PNP-D-mAb treated tumors displayed strong signals of DOX and Cy5.5, with the signal of Cy5.5-labeled antibodies being highly concentrated into the cells with fiber-like shapes, which may correspond to the CAFs. To further test the penetration capability in vivo, effects of various formulations with the same dose of DOX (5 mg kg^{-1}) on tumor-bearing mice were investigated. 24 h after the intravenous injection, the DOX fluorescence in the frozen slices was measured under the same condition (Figure S11, Supporting Information). The tumors from the PNP-D-mAb treated mice exhibited the strongest fluorescence signal compared to those from other groups, indicating effective tumor penetration of the drug.

Next, we evaluated the in vivo antitumor efficacy of these DOX nanoformulations after subcutaneously coimplanting CAFs and PC-3 cells in nude mice.[20,43,44] Although the coimplanted tumor model cannot fully reflect the complicated features of tumor microenvironment, we utilized this simple model to ensure the presence of CAFs in the xenograft tumors and to directly demonstrate the CAF-targeted therapeutic effect of our nanoparticles. When tumors grew to 200 mm^3 on average, we randomly divided the tumor-bearing mice into six groups (8 mice/group) which were treated with saline (control), PNP, DOX, PNP-D, PNP-D-IgG or PNP-D-mAb through tail vein injection every three days. Each formulation had equal dosage of DOX (3 mg kg^{-1}). Tumor volume was measured daily from each mouse at the same time. From the tumor growth curve, we observed that tumors in the PNP-D-mAb treated group ceased to grow after treatment and shrank gradually (Figure 4B, Figure S12, Supporting Information), underlining the promising tumor suppression efficiency of our nanocarrier granted by its strong tumor targeting and cell penetrating ability; tumors in PNP-D-IgG treated group grew slightly slower than the control and the PNP treated group, probably due to the low drug penetration; PNP-D with multiple positive charges achieved nonideal antitumor effect probably due to the RES-mediated nonspecific clearance; free DOX, without any tumor targeting capacity, suppressed tumor growth to certain extent but less efficient than PNP-D-mAb. After four treatments, the tumor tissue sections were analyzed by H&E staining for evaluation of the morphology, immunohistochemical labeling of CAFs by mouse anti-human α-smooth muscle actin monoclonal antibody (α-SMA),[45,46] and terminal deoxynucleotidyl transferased dUTP nick end labeling (TUNEL) assay for detection of apoptosis (Figure 4C). Compared to the control group, free DOX and PNP-D treatment caused mild changes of tissue morphology, CAFs amount and apoptosis in tumors, which was consistent with their impotent antitumor efficacy. PNP-D-IgG treated tumors showed almost no change in above three indexes. Excitingly, the morphology of tumors in the PNP-D-mAb treated group experienced dramatic changes, with most cells in apoptotic state. α-SMA labeling revealed the disappearance of the typical morphology of CAFs in the PNP-D-mAb treated tumors. The percentage of apoptotic cells in each group determined by TUNEL staining also supported the observations above (Figure 4D), as the TUNEL-positive cells in PNP-D-mAb treated tumors were about 60%, while other groups were much lower (control: 5%, DOX: 15%, PNP-D: 17%, PNP-D-IgG: 7%). The numbers of typical CAFs were analyzed by counting α-SMA positive cells from the α-SMA stained tumor slices (Figure 4E), and each group was from five random fields observed under a light microscope. Rare typical morphology of CAFs can be observed in PNP-D-mAb treated tumor slices compared to other groups. These results strengthened our conclusion that the dual-mode nanomaterial PNP-D-mAb with targeting and high penetration features can achieve maximum antitumor effect through depletion of CAFs stromal barrier. Neverthless, tumor microenvironment is a sophisticated ensemble comprising various types of stromal cells besides CAFs. Further in-depth study on the effects of PNP-D-mAb on other stromal cells, such as tumor vasculatures and immune cells may provide ample information to represent a more complete picture about the tumor microenvironment.

Considering the cardiotoxicity of DOX and the distribution of PNP-D-mAb in liver for a certain period,[47] we analyzed the morphology of hearts and livers from above treated tumor-bearing mice by H&E staining. No obvious morphological changes in hearts and livers were observed in any drug-formulation treated groups compared to the mice without treatment (Figure S13, Supporting Information). Meanwhile,

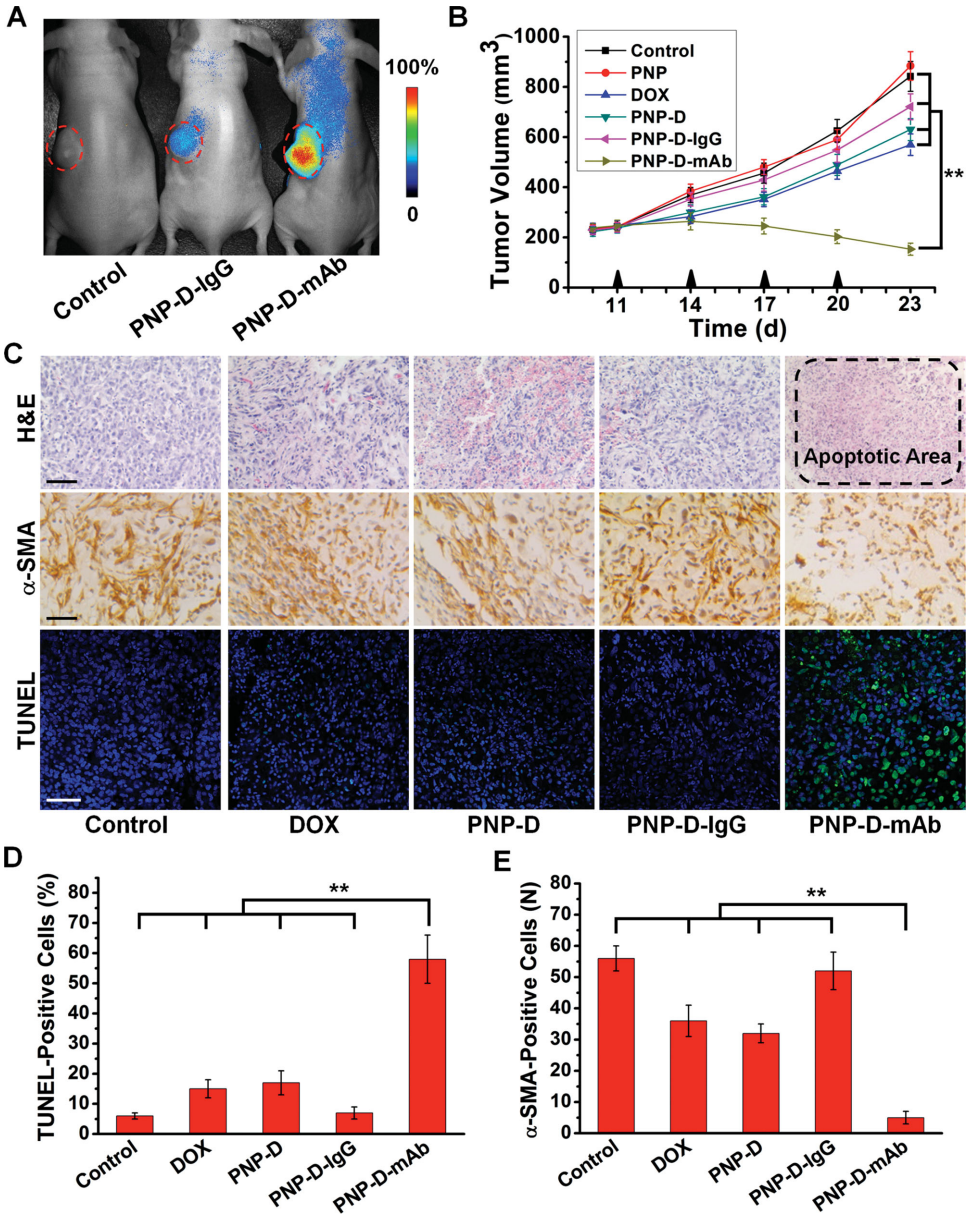

Figure 4. Tumor targeting and therapeutic efficacy of DOX-loaded nanoparticles in vivo. A) Near-infrared (NIR) tumor imaging of the Cy5.5-labeled PNP-D-IgG and PNP-D-mAb in vivo. The dose of DOX in each mouse was 5 mg kg^{-1}. B) Growth curves of tumors treated by various DOX formulations. The dose of DOX was 3 mg kg^{-1}. Data are presented as mean ± S.D. ($n = 8$). $^{**}p < 0.01$ versus control, DOX, PNP-D, and PNP-D-IgG. C) Analysis of tumor slices treated with differnt DOX formulations. H&E staining, the first row; α-SMA immunohistochemical staining, the middle row; TUNEL immunofluorescence staining, the last row, blue: DAPI, green: FITC-TUNEL. Scale bars, 50 μm. D) Quantification of the percentage of TUNEL positive apoptotic cells in tumors treated by various DOX formulations. The percent of apoptotic cells among the total cells in each field was calculated. Five random fields were observed for each tumor under a confocal microscope. Data are presented as mean ± S.D. $^{**}p < 0.01$ versus control, DOX, PNP-D, and PNP-D-IgG. E) Numbers of α-SMA positive cells in tumors treated by various DOX formulations. Five random fields were observed for each α-SMA stained tumor slice under a light microscope. The brown stained fibroblasts were taken into account. Data are presented as mean ± S.D. $^{**}p < 0.01$ versus control, DOX, PNP-D, and PNP-D-IgG.

we examined several biochemical indicators (myocardial isoenzyme of creatine kinase, CK-MB; creatine kinase, CK; lactate dehydrogenase, LDH; aspartate transaminase, AST; alanine aminotransferase, ALT; direct bilirubin, DBIL; total bilirubin, TBIL) related to myocardial function (Figure S14A–C, Supporting Information) and liver function (Figure S14D,E, Supporting Information) in serum and found significant variation. On one side, fast growth of the tumor xenografts significantly influenced some biochemical indicators compared to normal mice (without tumor burden), including abnormal high levels of LDH, DBIL, and TBIL. On the other side, free DOX exhibited toxicity to myocardium and liver cells, causing

the reduction of CK-MB and CK related with the low energy transport in myocardium,[48] and the obvious increase in AST and ALT, representatives of liver cell damage.[49,50] The levels of these indicators in PNP-D-IgG treated mice were similar to those in nontreated tumor-bearing mice, suggesting the marginal side effect as well as therapeutic efficacy of PNP-D-IgG. Strikingly, the indicator levels of the PNP-D-mAb treated mice resembled those of the normal mice. These results implied that PNP-D-mAb not only achieved significant antitumor efficacy but also attenuated the adverse effect of DOX.

In summary, we have successfully engineered a novel two-step dual-mode nanomaterial referred to as PNP-D-mAb, with specific tumor targeting and enhanced penetration capacity. Our results strongly support the notion that the essential features of PNP-D-mAb, CAFs targeting combined with increased cellular uptake coordinated by CPP and cholesterol, resulted in excellent amelioration of the antitumor efficacy of a chemotherapeutic drug, DOX. This nanomaterial improved the penetration of DOX into the tumor tissues by depletion of CAFs and breakage of the stromal barrier. Compared to free drug and its nontargeting equivalent, PNP-D-mAb exhibited superior tumor penetrating ability and antitumor activity as well as low side effects. By targeting specific stromal cells in the tumor microenvironment and improving cellular uptake, the current study lays a foundation for further development of such combination strategy for drug delivery against a wide range of solid tumors.

Supporting Information

Supporting Information is available from the Wiley Online Library or from the author.

Acknowledgments

T.J., Y.D. contributed equally to this work. The authors thank Professor Ju Zhang from Nankai University for providing PF179T-CAF cell line and Juan Liu from Professor Liang's laboratory at NCNST for providing flow cytometry service. This work was supported by the grants from MoST 973 (Grant Nos. 2012CB934004, 2011CB933400, 2012CB917103, and 2013CB932700), the grants from NSFC (Grant Nos. 31325010, 31170962, 51203032, 21373067, and 31300822) and the Key Research Program of Chinese Academy of Sciences (Grant No. KGZD-EW-T06).

Received: October 11, 2014
Revised: January 14, 2015
Published online: February 4, 2015

[1] D. A. Scheinberg, C. H. Villa, F. E. Escorcia, M. R. McDevitt, *Nat. Rev. Clin. Oncol.* **2010**, *7*, 266.
[2] T. Ji, Y. Zhao, Y. Ding, G. Nie, *Adv. Mater.* **2013**, *25*, 3508.
[3] O. C. Farokhzad, R. Langer, *Adv. Drug Delivery Rev.* **2006**, *58*, 1456.
[4] D. Sutton, N. Nasongkla, E. Blanco, J. M. Gao, *Pharm. Res.* **2007**, *24*, 1029.
[5] A. Maksimenko, F. Dosio, J. Mougin, A. Ferrero, S. Wack, L. H. Reddy, A. Weyn, E. Lepeltier, C. Bourgaux, B. Stella, L. Cattel, P. Couvreur, *Proc. Natl. Acad. Sci. USA* **2014**, *111*, E217.
[6] V. P. Chauhan, R. K. Jain, *Nat. Mater.* **2013**, *12*, 958.
[7] D. Peer, J. M. Karp, S. Hong, O. C. Farokhzad, R. Margalit, R. Langer, *Nat. Nanotechnol.* **2007**, *2*, 751.
[8] R. K. Jain, *Annu. Rev. Biomed. Eng.* **1999**, *1*, 241.
[9] S. Su, H. Wang, X. Liu, Y. Wu, G. Nie, *Biomaterials* **2013**, *34*, 3523.
[10] T. Wei, J. Liu, H. Ma, Q. Cheng, Y. Huang, J. Zhao, S. Huo, X. Xue, Z. Liang, X. J. Liang, *Nano Lett.* **2013**, *13*, 2528.
[11] H. Wang, Y. Zhao, Y. Wu, Y. Hu, K. Nan, G. Nie, H. Chen, *Biomaterials* **2011**, *32*, 8281.
[12] H. Wang, Y. Wu, R. Zhao, G. Nie, *Adv. Mater.* **2013**, *25*, 1616.
[13] B. Yameen, W. I. Choi, C. Vilos, A. Swami, J. Shi, O. C. Farokhzad, *J. Controlled Release* **2014**, *190*, 485.
[14] N. Erez, M. Truitt, P. Olson, D. Hanahan, *Cancer Cell* **2010**, *17*, 135.
[15] R. Kalluri, M. Zeisberg, *Nat. Rev. Cancer* **2006**, *6*, 392.
[16] T. D. Tlsty, L. M. Coussens, *Annu. Rev. Pathol.: Mech. Dis.* **2006**, *1*, 119.
[17] J. J. Tomasek, G. Gabbiani, B. Hinz, C. Chaponnier, R. A. Brown, *Nat. Rev. Mol. Cell Biol.* **2002**, *3*, 349.
[18] G. Parsonage, A. D. Filer, O. Haworth, G. B. Nash, G. E. Rainger, M. Salmon, C. D. Buckley, *Trends Immunol.* **2005**, *26*, 150.
[19] H. Y. Chang, J. T. Chi, S. Dudoit, C. Bondre, M. Rijn, D. Botstein, P. O. Brown, *Proc. Natl. Acad. Sci. USA* **2002**, *99*, 12877.
[20] Z. Liu, A. Ivanoff, J. Klominek, *Int. J. Cancer* **2001**, *91*, 638.
[21] T. Stylianopoulos, J. D. Martin, V. P. Chauhan, S. R. Jain, B. Diop-Frimpong, N. Bardeesy, B. L. Smith, C. R. Ferrone, F. J. Hornicek, Y. Boucher, L. L. Munn, R. K. Jain, *Proc. Natl. Acad. Sci. USA* **2012**, *109*, 15101.
[22] D. J. Mitchell, D. T. Kim, L. Steinman, C. G. Fathman, J. B. Rothbard, *J. Peptide Res.* **2000**, *56*, 318.
[23] S. Futaki, T. Suzuki, W. Ohashi, T. Yagami, S. Tanaka, K. Ueda, Y. Sugiura, *J. Biol. Chem.* **2001**, *276*, 5836.
[24] S. Futaki, *Adv. Drug Delivery Rev.* **2005**, *57*, 547.
[25] L. Liu, K. Xu, H. Wang, J. Tan, P. K. Jeremy, W. Fan, S. S. Venkatraman, L. Li, Y.-Y. Yang, *Nat. Nanotechnol.* **2009**, *4*, 457.
[26] R. G. Weiss, *Tetrahedron* **1988**, *44*, 3413.
[27] M. Lee, J. Rentz, S. O. Han, D. A. Bull, S. W. Kim, *Gene Therapy* **2003**, *10*, 585.
[28] J. X. Chen, H. Y. Wang, C. Li, K. Han, X. Z. Zhang, R. X. Zhuo, *Biomaterials* **2011**, *32*, 1678.
[29] R. Romberg, W. E. Hennink, G. Storm, *Pharm. Res.* **2008**, *25*, 55.
[30] A. Albanese, P. S. Tang, W. C. W. Chan, *Annu. Rev. Biomed. Eng.* **2012**, *14*, 1.
[31] F. Alexis, E. Pridgen, L. K. Molnar, O. C. Farokhzad, *Mol. Pharmaceutics* **2008**, *5*, 505.
[32] J. E. Park, M. C. Lenter, R. N. Zimmermann, P. Garin-Chesa, L. J. Old, W. J. Retting, *J. Biol. Chem.* **1999**, *274*, 36505.
[33] O. Abbas, J. E. Richards, M. Mahalingam, *Mod. Pathol.* **2010**, *23*, 1535.
[34] J. Zhang, J. Liu, *Pharmacol. Ther.* **2013**, *137*, 200.
[35] P. Cirri, P. Chiarugi, *Cancer Metast Rev.* **2012**, *31*, 195.
[36] J. A. Hubbell, R. Langer, *Nat. Mater.* **2013**, *12*, 963.
[37] F. Danhier, O. Feron, V. Préat, *J. Controlled Release* **2010**, *14*, 135.
[38] V. P. Torchilin, R. Rammohan, V. Weissig, T. S. Levchenko, *Proc. Natl. Acad. Sci. USA* **2001**, *98*, 8786.
[39] F. Madani, S. Lindberg, U. Langel, S. Futaki, A. Gräslund, *J. Biophys.* **2011**, *2011*, 1.
[40] N. Schmidt, A. Mishra, G. H. Lai, G. C. L. Wong, *FEBS Lett.* **2010**, *584*, 1806.
[41] R. Kugler, O. Bouloussa, F. Rodelez, *Microbiology* **2005**, *151*, 1341.
[42] A. M. Carmona-Ribeiro, L. D. De Melo Carrasco, *Int. J. Mol. Sci.* **2013**, *14*, 9906.

[43] R. F. Hwang, T. Moore, T. Arumugam, V. Ramachandran, K. D. Amos, A. Rivera, B. Ji, D. B. Evans, C. D. Logsdon, *Cancer Res.* **2008**, *68*, 918.
[44] E. Giannoni, F. Bianchini, L. Masieri, S. Serni, E. Torre, L. Calorini, P. Chiarugi, *Cancer Res.* **2010**, *70*, 6945.
[45] S. E. Holton, M. J. Walsh, A. Kajdacsy-Balla, R. Bhargava, *Biophys. J.* **2011**, *101*, 1513.
[46] M. Bauer, G. Su, C. Casper, R. He, W. Rehrauer, A. Friedl, *Oncogene* **2010**, *29*, 1732.
[47] Y. W. Zhang, J. Shi, Y. J. Li, L. Wei, *Arch. Immunol. Ther. Exp.* **2009**, *57*, 435.
[48] I. Oudman, J. F. Clark, L. M. Brewster, *PloS ONE* **2013**, *8*, e52879.
[49] G. Khan, S. E. Haque, T. Anwer, M. N. Ahsan, M. M. Safhi, M. F. Alam, *Acta Pol. Pharm.* **2014**, *71*, 861.
[50] I. Salouege, R. Ben Ali, D. B. Said, N. Elkadri, N. Kourda, M. Lakhal, A. Klouz, *J. Cancer Res. Ther.* **2014**, *10*, 274.